

Broadband pump-probe study of biexcitons in chemically exfoliated layered WS₂

R. K. Chowdhury,¹ S. Nandy,¹ S. Bhattacharya,¹ M. Karmakar,¹ B. N. S. Bhaktha,¹ P. K. Datta,¹ A. Taraphder,^{1,2} and S. K. Ray^{1,3}

¹*Department of Physics, Indian Institute of Technology Kharagpur, Kharagpur - 721302, India*

²*Centre for Theoretical Studies, Indian Institute of Technology Kharagpur, W.B. 721302, India*

³*S. N. Bose National Centre for Basic Sciences, Kolkata 700106, India*

Strong light-matter interactions in layered transition metal dichalcogenides (TMDs) open up vivid possibilities for novel exciton-based devices. The optical properties of TMDs are dominated mostly by the tightly bound excitons and more complex quasiparticles, the biexcitons. Instead of physically exfoliated monolayers, the solvent-mediated chemical exfoliation of these 2D crystals is a cost-effective, large-scale production method suitable for real device applications. We explore the ultrafast excitonic processes in WS₂ dispersion using broadband femtosecond pump-probe spectroscopy at room temperature. We detect the biexcitons experimentally and calculate their binding energies, in excellent agreement with earlier theoretical predictions. Using many-body physics, we show that the excitons act like Weiner-Mott excitons and explain the origin of excitons via first-principles calculations. Our detailed time-resolved investigation provides ultrafast radiative and non-radiative lifetimes of excitons and biexcitons in WS₂. Indeed, our results demonstrate the potential for excitonic quasiparticle-controlled TMDs-based devices operating at room temperature.

I. INTRODUCTION

Transition metal dichalcogenides (TMDs), playing a leading role in the development of two dimensional (2D) semiconducting physics, exhibit superior optical properties that are substantially different from their bulk contribution^{1,2}. In the family of 2D TMDs, one of the most extensively studied material is tungsten disulphide (WS₂) that displays a wide variety of intriguing properties such as layer-tunable band gap modulation, large spin-valley splitting, high absorption coefficient and ultrafast excitonic properties³⁻⁷. Most importantly, one can tune the properties by varying the number of layers, which makes this material a promising candidate for novel device applications. Using variable range of architectures, WS₂ is being constantly explored for low-cost, sensitive and scalable optoelectronic devices like ultra-high responsive photosensors, valleytronics, and excitonic devices⁸⁻¹².

In general, atomically thin WS₂, consisting of two hexagonally bonded sulfur (S) atoms, bonded with transition metal tungsten (W), get stacked by weak van der-Waals force of attraction analogous to graphene¹³. As a result of this weak interaction, 2D layered WS₂ can be exfoliated readily that results in layer-dependent tunable energy band structure resulting in direct band gap transition for the monolayer. The layered WS₂ also exhibits unique phenomenon called band nesting (BN), where the valance band (VB) and conduction band (CB) are parallel to each other along a specific k-path (towards Γ -K direction). Due to the BN effect, the photo-generated charge carriers with opposite polarities move with equal but opposite velocities in the CB and VB, exhibiting extraordinary optical characteristics as reported earlier¹⁴. Furthermore, unlike conventional semiconductors, Coulomb interaction in TMDs is remarkably robust because of the excited carrier screening and Pauli blocking^{15,16,18,19}. As a result, various excitonic quasiparticles like exciton, biexciton (two neutral excitons bound by in-

teraction) are predicted to co-exist inside the exfoliated 2D stratum at room temperature²⁰⁻²⁸. The steady-state optical studies are incapable to reveal the nature of these excitonic phenomena and therefore, time-resolved optical studies are required to investigate the ultrafast carrier dynamics of layered WS₂.

On the other hand, as compared to physical exfoliation, chemical vapor deposition (CVD) and solvent-mediated chemical exfoliation techniques of 2D TMDs are contemporaneous in terms of wafer-scale production, though the last one appears to be cost-effective for device applications^{13,29,30}. Therefore, chemically exfoliated mono-to-few layer WS₂ has been widely used for the nanofabrication of various optoelectronic components^{31,32}. However, the manifestation of the devices for futuristic applications requires a profound knowledge of the excitonic energy levels, formation and evolution of multiexcitonic states and their decay dynamics, which are still lacking^{33,34}. In the present work, we have chosen the time-resolved pump-probe spectroscopy of chemically exfoliated WS₂ layers to study the above ultrafast processes in detail.

We have explained the transient absorption spectroscopy (TAS) signals of chemically exfoliated mono-to-quad layer WS₂ flakes dispersed in dimethylformamide (DMF) solvent in the following. A horizontally polarized optical pump (405 nm, 3 eV) with varying power along with a broadband (350-750 nm) optical probe was used for the ultrafast pump-probe measurements. The Raman fingerprint have confirmed the exfoliation of mono-to-quad layer of WS₂ flakes in DMF. Using density functional theory (DFT) calculations, we have also shown that the degeneracy and splitting of VB at different k-points are always present, which are similar in nature specially at K and K' points in the presence of atomic spin-orbit coupling from mono-to-quad layer transformation. Our theoretical calculations suggest that the physical reasons for the generation and evolution of excitons, biexcitons and their corresponding decay dynam-

ics do not change with increase in number of layers up to quadlayers. Furthermore, a detailed investigation of TAS signal of the layered WS_2 dispersion confirms six major features - (i) three saturation absorptions (SA) which are governed by steady state UV-Vis absorption and (ii) three excited state absorptions that substantiate the presence of excitonic quasiparticles like excitons and biexcitons. TAS spectra confirm that the relative oscillator strength of the deconvoluted biexcitonic peaks increases with probe delay with respect to the excited state absorption (ESA), which is discussed in terms of hot exciton cooling process. The binding energies of AA (~ 69 meV) and BB (~ 66 meV) biexcitons have been calculated experimentally from blue shifted biexcitonic peaks. We have also measured the power dependent red-shift of the biexcitonic peak, which is the result of many-body interactions governed by excited state screening and reduction of excitonic band-gap due to band renormalization at higher pump excitations^{18,19,35,36}. The ultrafast non-radiative and radiative lifetimes of the excitons and biexcitons have also been extracted using 3rd exponentially fitted transient absorption spectra.

II. METHODS

A. Sample synthesis

For the synthesis of WS_2 , we have used the exfoliation technique mentioned in the earlier reports from our group^{29,37}. Resulting flakes have a lateral dimension ranging from a few hundred nanometers to a micron with ~ 1 -4 layers WS_2 flakes dispersed uniformly in DMF solvent as confirmed by Raman analysis.

B. Raman and steady state absorption characterization

Raman spectra of WS_2 on silicon were recorded using a T64000 (JobinYvon Horiba) spectrometer with an Argon-Krypton mixed ion gas laser (514.5 nm). The absorption spectra of the dispersion of layered WS_2 were acquired using a PerkinElmer Lambda-2 spectrometer in a wavelength range of 190-1100 nm.

C. Transient absorption spectroscopy

Ultrafast transient absorption spectra of WS_2 dispersion is recorded with a commercially available transient absorption spectrometer (Newport) using 50 fs Ti: Sapphire mode locked amplifier (Libra-He, Coherent) with 808 nm center wavelength and repetition rate of 1 kHz. Major part (70%) of the fundamental beam goes into optical parametric amplifier (TOPAS prime, Coherent), which acts as tunable pump source. The other part of

the fundamental beam is focused in a 3 mm CaF_2 crystal which generates linearly polarized white light continuum (350-750 nm) probe. The latter one passes through an optical delay channel using a motorized translational stage in order to probe the system at different times after the pump excitation has perturbed the system. Pump and probe beam spot-sizes are maintained at 2 mm and 0.16 mm respectively which is used for this non-collinear pump-probe measurement setup. This kind of arrangements provide the pump fluence as 1.8 GW/cm^2 for 3 mW time averaged pump power. A spectrometer equipped with linear Si photodiode array is used to detect the differential probe spectra. Differential absorbance (ΔA) spectra are measured by modulating the pump beam at 500 Hz with an optical chopper which is again fed to the spectrometer.

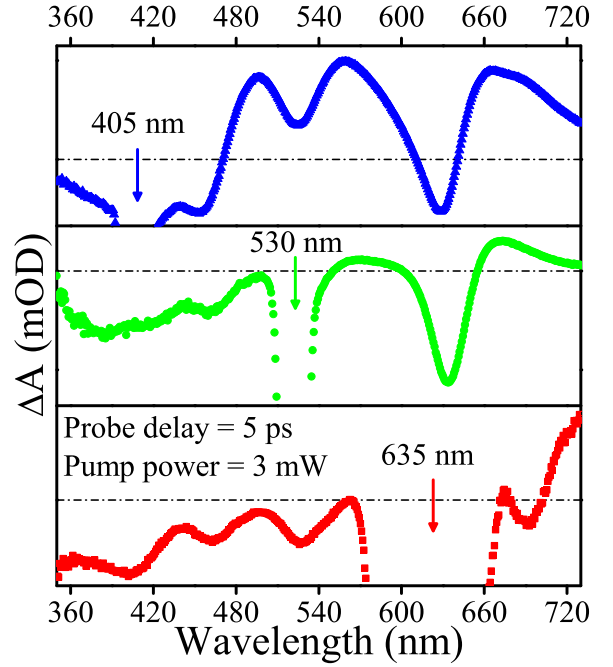


FIG. 1. (Color online) TAS spectra of mono-to-quad layer dispersion of WS_2 , recorded at fixed probe delay $t = 5$ ps, for three pump excitation (3 mW) wavelengths, i.e., in resonance with the A ($\lambda_{\text{pump}} = 635$ nm) and B ($\lambda_{\text{pump}} = 530$ nm) excitons, and out of resonance with C ($\lambda_{\text{pump}} = 405$ nm).

D. Resonant and off-resonant pump excitation.

TAS spectra have been obtained for different pump excitation wavelengths starting from 405 nm, i.e. higher than the A, B and C excitonic wavelength, along with two other excitation (635 nm and 530 nm) resonant with A and B respectively (Fig. 1). Interestingly, all the six major spectral features (SA and ESA) are still observed for the lower energy resonant pumping conditions. The

SA at B for the excitation at A ($\lambda_{pump} = 635$ nm) can be explained by extremely fast intervalley spin relaxation at K and K' points. The unexpected presence of the higher energy C proves that all the three excitons (A, B and C) are resonantly coupled with each other.

E. Computational Details

The electronic band structure calculations of monolayer, bilayer, trilayer and quadlayer WS₂ have been performed in the framework of ab initio density functional theory (DFT) in conjunction with all-electron projector augmented wave potentials and the Perdew-Burke-Ernzerhof generalized gradient approximation (PBE-GGA)⁵⁴ to the electronic exchange and correlation, as implemented in the WIEN2K code⁵⁵, which has been used successfully in various instances for describing low-dimensional systems. We incorporate the atomic spin orbit coupling with GGA calculation in terms of the second-variational method with scalar-relativistic orbitals as a basis. For all four cases, we have created a periodic slab geometry with a 20-Å-thick vacuum layer along Z axis. We have relaxed both the in-plane lattice constant **a** and the positional parameter **z** until the force on every atom becomes less than 2 mRy/Bohr. We have taken the same values of $R_{mt} = 2.1$ a.u., $R_{mt}K_{max} = 8$, and $l_{max} = 12$ and same exchange-correlation functional in each calculation. We have employed a k-mesh of $39 \times 39 \times 2$ for the monolayer, $34 \times 34 \times 3$ for bilayer, $30 \times 30 \times 1$ for trilayer, and $31 \times 31 \times 1$ for quadlayer system. The monolayer of WS₂, composed of single S-W-S stacking unit, has a threefold rotational axis (c axis). Due to lack of inversion symmetry with respect to the mirror plane (containing the W atoms), the symmetry properties of monolayer and trilayer WS₂ are described by a space group 187-P6m2 (D_{3h}^1) compared to bilayer and quadlayer which have a space group 164-P3m1 (D_{6h}^4).

III. RESULTS

A. Identification of number of S-W-S Layers in Dispersion

Raman fingerprints can provide the information of different phonon modes that can accurately quantify the number of S-W-S layers in the sample. The Raman intensity ($\lambda_{ex} = 514.5$ nm) of $A_{1g}(\Gamma)$ phonon mode monotonically diminishes, whereas the 2nd order longitudinal acoustic (2LA(M)) phonon mode drastically increases with the decrease of layer numbers as shown in Fig. 2(a) and (b). The intensity ratio (I_{2LA}/I_{A1g}) of these two Raman modes can unambiguously identify the exact number of S-W-S layers present in the sample³⁸. We have spin coated the dispersion of WS₂ on Si substrates and acquired the Raman signal at several positions. The intensity ratio (I_{2LA}/I_{A1g}) histogram (Fig. 2(c)) ranging

from 0.85 to 1.45 for different sample position confirms that we have successfully synthesized \sim mono-to-quad WS₂ layers dispersed in DMF solvent.

B. Biexciton Formation

Unlike conventional semiconductors, biexcitons in WS₂ usually form in a two-steps (ground state-intermediate pseudo excitonic states-biexcitonic state) process governed by cumulative effect of pump and probe photons^{39,40} as shown in Fig. 3 (a). In WS₂, the intermediate pseudo excitonic state appears due to valley splitting^{16,26}. As a result of this, different kind of biexcitons form namely AA and BB biexcitons. The biexcitonic features of WS₂ can be realized directly from TAS spectra in the following manner. The deconvoluted steady state absorption spectrum is depicted in Fig. 3(b), whereas the 3D contour plot of the TAS signal as a function of probe wavelength (420-750 nm) and delay (-5 to 300 ps) is depicted in Fig. 3(c) for mono-to-quad layer WS₂ dispersion in DMF solvent. The TAS spectrum shows six major features including three saturated absorption (SA) peaks and three excited state absorption (ESA) peaks along with a pump (405 nm, 3 mW) induced ground state bleaching (GSB). The saturation absorption peaks at three different positions, A (456 nm), B (525 nm), and C (633 nm) corroborate with the deconvoluted steady state absorption peaks of the sample. To distinguish the biexcitonic features from ESA, TAS spectra are deconvoluted using multiple gaussian fit as shown in Fig. 4(a)-(d). Six gaussian peaks are used to reproduce the complete TAS spectra at different probe delays where the center position of negative gaussian peaks are kept fixed at different wavelengths of steady state excitonic absorption peaks (A, B and C). The positive ΔA features as depicted in Fig. 3(c) at two different positions 659 nm (peak 1) and 563 nm (peak 2), calculated from deconvoluted peak of TAS signal (Fig. 4(a)-(d)) suggest the biexciton formation. The broadening effect of these peaks are attributed to intervalley biexcitonic absorptions¹⁶. In our experiment, the off-resonant deep conduction band excitation (405 nm or 3 eV) by the pump pulse ($h\nu > E_A$) imparts an excess energy per exciton (δE), where E_A is the energy of the exciton, leads to the immediate formation of hot exciton gas. The biexciton energy can now be expressed as,

$$E_{XY} = (E_X + \delta E)_{pump} + (E_Y - \Delta - \delta E)_{probe} \quad (1)$$

where E_X and E_Y are the energy of the X and Y excitons respectively and Δ is the biexciton binding energy¹⁶. Thus the biexcitonic peaks are shifted from the corresponding excitonic peak with a Δ amount of energy. On the other hand, the origin of peak 3 (503 nm) as shown in Fig. 3(c) is possibly different, which seems to be just another excited state absorption (ESA) as there is no corresponding steady state absorption (Fig. 3(b)).

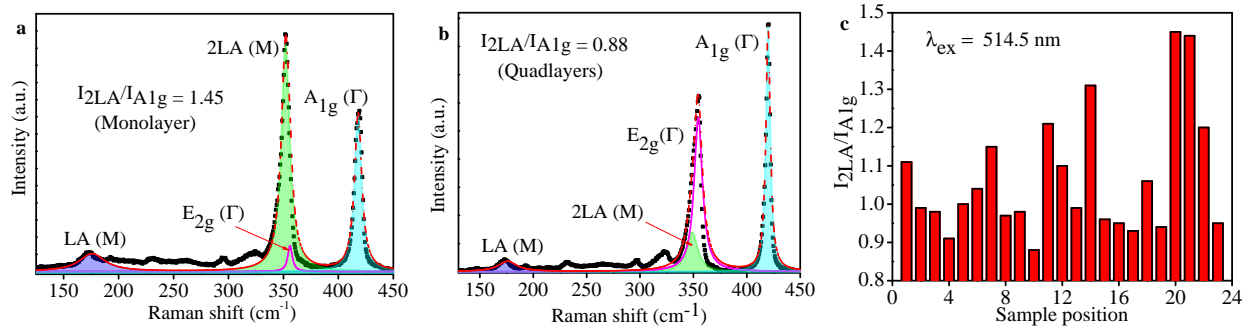


FIG. 2. (Color online) Raman characterizations of exfoliated WS_2 show the signature of (a) monolayer and (b) quadlayers. The deconvoluted spectra consist of 1st order (blue shaded region) and 2nd order (green shaded region) LA modes along with different vibrational modes (E_{2g} as pink line and A_{1g} as cyan shaded region). (c) The intensity ratios of 2nd order LA and A_{1g} modes at different positions of the sample confirm the number of exfoliated S-W-S layers (mono-to-quad).

C. Exciton cooling process

We have acquired the transient absorption spectra for different probe time delays for further elaboration of the biexciton formation. The TAS signals at different time delays (5 ps, 100 ps, 300 ps and 1 ns) along with deconvoluted peaks are depicted in Fig. 4(a)-(d). It is clearly seen from the Fig. 4(a)-(d) that the position of negative peaks (A, B and C) originating from saturation absorption (SA) remain fixed with delay. In presence of pump, the photo-bleached ground states are unable to absorb the probe pulse. As a result, probe directly transmits to detector and position of the negative peaks remain unchanged. On the other hand, we have found that ESA continuously decreases from 5 ps to 300 ps and gets saturated later on, as shown in Fig. 4(a)-(d). Relative enhancement of oscillator strength of different blue-shifted biexcitonic peaks with respect to ESA are observed with increase in probe delay. Here, the shift is driven by exciton cooling process⁴¹. The measured probe delay dependent blue-shift for biexcitonic peak (containing BB) is ~ 90 meV⁴² from 5 ps to 300 ps which remains unchanged up to 1 ns. The hot exciton gas gradually relaxes into the cold exciton gas via releasing energy (δE_{probe}) to the WS_2 lattice and DMF solvent. As a result, during the formation of cold exciton gas, the energy of the biexciton population (E_{XY}) shifts into lower wavelengths with increasing delay. Using these cooling process, we have also calculated the biexciton binding energies (Tab. I) as ~ 69 meV (AA) and 66 meV (BB) from the difference between the blue shifted biexcitonic peaks and corresponding excitonic (SA) peaks for 1 ns delay using Eq. 1 which closely matches with previous theoretical and experimental reports on WS_2 ^{26,39,40}.

D. Many-body interactions

We find that biexcitons are formed at room temperature for the studied system due to strong many body in-

Biexciton	Δ (meV)
AA	69
BB	66

TABLE I. Binding energies of AA and BB biexcitons in layered WS_2

teractions which results into red-shift of biexcitonic peaks with increasing pump power. To verify this strange behavior, we acquire series of ΔA (Fig. 5(a)) for different pump (405 nm, 3 eV) photon energies at 5 ps probe delay. The 5 ps time delay has been chosen, as the intervalley spin relaxation occurs in a time scale within a few hundreds of femtoseconds⁴³. As we are interested in biexciton formation process, we will focus on the 500-700 nm probe range of TAS signal. When the pump power is increased gradually from 50 μW to 4 mW (0.03 to 2.4 GW/cm^2), the positive peaks shift to lower energies and develop a low-energy shoulder as shown in Fig. 5. With increasing pump power, the number of biexciton formation enhances due to increase of exciton population, results into red shift of the biexcitonic peaks^{16,17}. The calculated red-shift of these two peaks are ~ 80 meV (BB) and ~ 90 meV (AA) for 3 mW pump power, with no additional shift up to 4 mW. At higher pump powers, the many body interactions get additionally screened by the photoexcited carriers and modify exchange-correlation energies. On the other hand, the electronic band structure becomes renormalized which causes the reduction of exciton binding energy as well as enhancement in absorption of pump photons^{16,21,35}. Since, the Coulomb interactions will tend to recombine the e-h pair and reduction of exciton binding energy due to band renormalization as well as the modified dielectric screening due to the distribution of S-W-S layer numbers will try to make them free^{18,19}. The trade off between these two effects often results in a net energy shift (ΔE) of the biexcitonic peak. The red shift (ΔE) of the biexcitonic peak can be

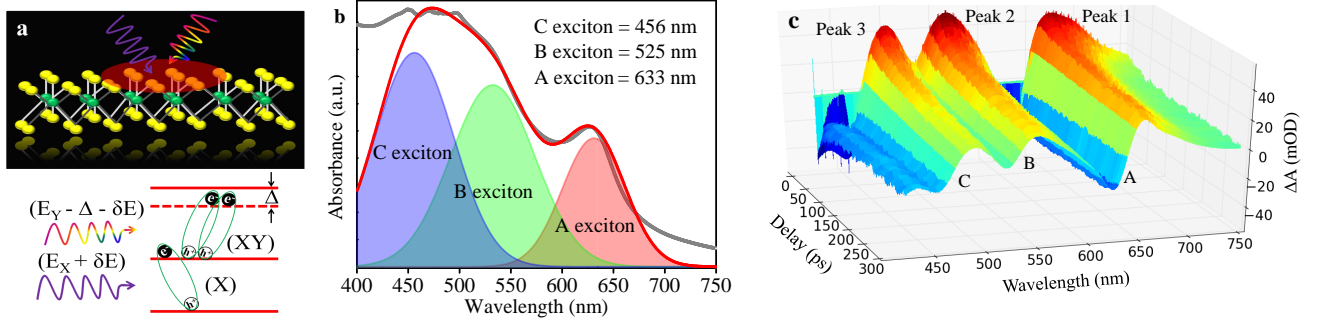


FIG. 3. (Color online) (a) Schematic representation of the formation of biexcitons in layered WS₂ using two-step pump ($E_X + \delta E$)-probe ($E_Y - \Delta - \delta E$) excitation process. Here excitons and biexcitons are defined as X and XY respectively. (b) depicts deconvoluted steady state absorption spectrum of WS₂ dispersion which clearly depicts the formation of A (red shaded region), B (green shaded region) and C (blue shaded region) excitons. (c) shows the contour map of TA signal for 405 nm, 3 mW pump excitation. Three saturation absorption valleys appear at the positions of steady state excitons (A, B and C), whereas three distinguish pump induced absorption peaks (peak 1, peak 2 and peak 3) appear in the contour map.

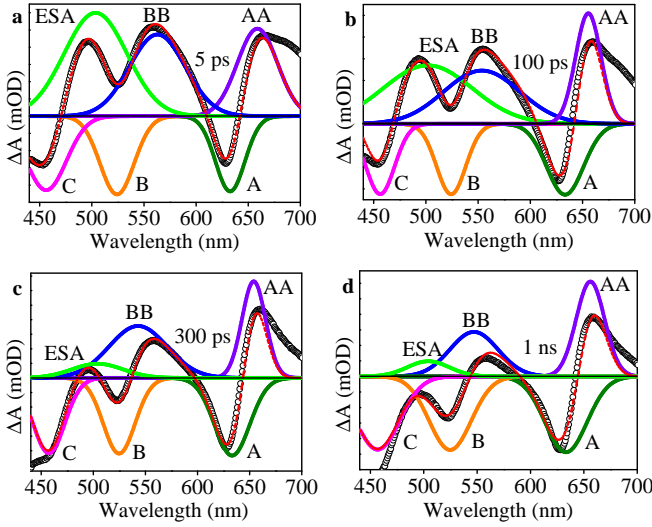


FIG. 4. (Color online) (a)-(d) show time resolved TA spectra of mono-to-quad layer WS₂ dispersion. The time delay has been varied from 5 ps to 1 ns (1000 ps). All four spectra show six major features containing three saturation absorption (C (pink line), B (orange line) and A (olive line)), two biexcitonic absorption (BB (blue line) and AA (violet line)) and one excited state absorption (green line).

calculated by the following equation,

$$\frac{\Delta E}{E_B} = \gamma(n\pi a_b^2)^k \quad (2)$$

where, E_B is the exciton binding energy, a_b is the exciton Bohr radius, k and γ are dimensionless factor. In Eq. (2), ΔE obeys a power-law nature with pump power (n), until the interexciton distance ($\propto \frac{1}{\sqrt{n}}$) approaches the exciton Bohr radius, where the Weiner-Mott excitonic transition is expected^{20,41}. It has been found that the short-range interactions will dominate for $\Delta E \propto \sqrt{n}$ whereas the long-range interaction becomes stronger for

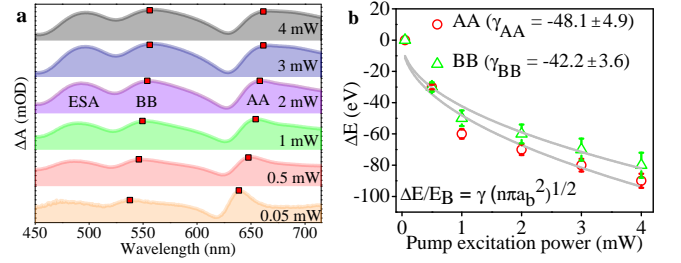


FIG. 5. (Color online) (a) shows pump (405 nm, 3 eV) power dependent (power increases from bottom to top) TA signals for 5 ps probe delay. The biexcitonic peaks are red shifted (red boxes) with increasing power up to 3 mW, whereas the peak positions of ESA remain unchanged. (b) shows variation of biexcitonic red shift (ΔE) with pump power for AA (red circle) and BB (green triangle) biexcitons. The data has been fitted by Eq. 2.

$\Delta E \propto n^{1/2}$. We find that the experimental results are best fitted with $k = 1/2$ and corresponding γ values are -48.1 ± 4.9 and -42.2 ± 3.6 for AA and BB, respectively as shown in Fig. 5(b). So, we are in such a situation where short-range interactions are dominant and the excitons are found to be Weiner-Mott excitons^{16,20}.

E. Origin of saturation absorption

The dispersion, used in this experiment, has the information of mono-to-quad layer of WS₂ as confirmed by Raman analysis. Therefore, it would be worth knowing whether SA peaks in TAS spectrum appears due to one particular layer or a combination of all layers of the WS₂ dispersion. To investigate the origin of SA peaks extracted from the pump-probe measurement, we have computed electronic band structure of monolayer, bilayer, trilayer and quadlayer WS₂ computed using first-principles calculations are shown in Fig. 6(a)-(d). Our

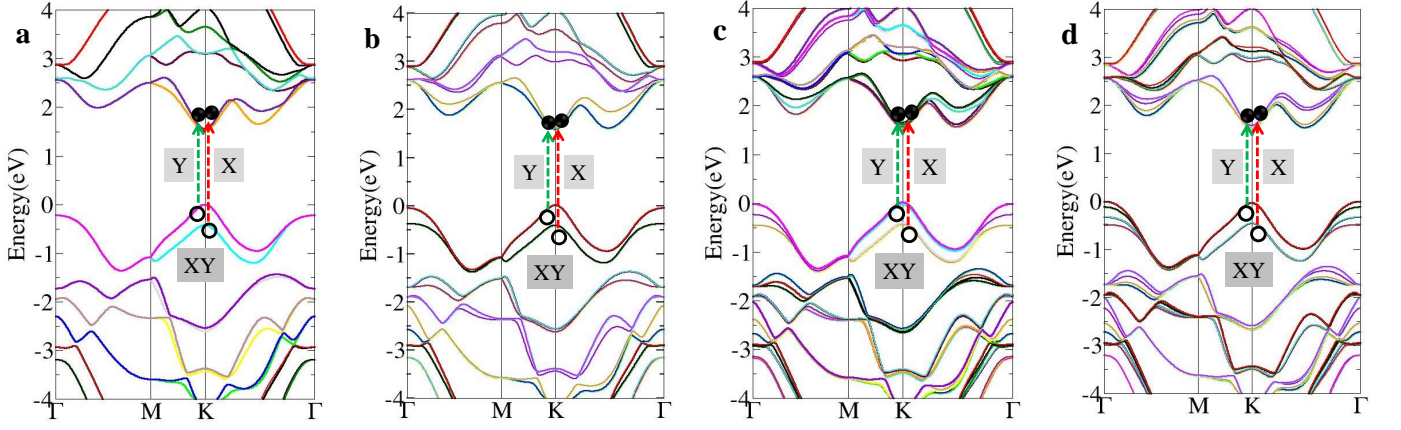


FIG. 6. (Color online) Electronic band structures calculated for the WS₂ (a) monolayer, (b) bilayer, (c) trilayer and (d) quadlayer systems with inclusion of the spin-orbit interaction. It is clear that the valence band splittings at K point are nearly independent of the number of layers. The biexciton formation via two-step pump-probe process is schematically shown for all four cases.

calculations reveal that the monolayer WS₂ is a direct-band-gap semiconductor with the valence band maxima (VBM) and conduction band minima (CBM) at K and K' point of the Brillouin zone, in contrast to the indirect band gap of the bilayer, trilayer and quadlayer WS₂, also observed in angle-resolved photoelectron spectroscopy experiment^{44–47}. In all four cases, the energy bands split at all k points except some points with special symmetry in the Brillouin zone due to the atomic spin-orbit coupling. The spin-orbit interaction breaks the spin degeneracy of the valence and conduction bands along the Γ -K-M direction. It is found that the splitting in VB is largest at the K point of the Brillouin zone whereas the CBM is also at K, as depicted in Fig. 6. The conduction band and valence band of WS₂ are composed of mainly d orbitals of W and relatively small admixture of p orbitals of S, which constitute spin splitting correspond to the K and K' valleys^{43,48}. The lifting of degeneracy in VB appears due to spin-orbit coupling in the E-K diagram for all four cases as shown in Fig. 6(a)-(d).

From our calculations, it is clear that the spin orbit interaction invoked valence band splitting, leads to energetically well-separated excitonic transitions which give rise to two distinct low-energy peaks at position A and B in the TAS spectrum as shown in Fig. 3(c). In this case, the pump pulse populates different valleys of conduction band. The electron population of one particular valley spreads over other valley due to inter-valley spin relaxation within a few hundred of femtoseconds, leads to the formation of dark excitons⁴³. Now, the SA peaks which appear mainly due to bright excitonic states, may also be present due to Pauli blocking of the dark excitonic states in the unpumped valleys in absence of pump^{49,50}.

On the other hand, the origin of C peak is different from A and B peaks. It is strongly believed that this peak appears due to steady state absorption from deep VB to CB²⁹. The detailed theoretical investigations re-

veal that the C peak actually originates from the locally parallel band along Γ -K direction which is also referred as band nesting (BN)¹⁴. The probability of excitonic transitions are governed by the joint density of states (JDOS)⁵¹ which can be written as

$$\rho^J(\omega) = \frac{1}{(2\pi)^2} \int_{S(\omega)} \frac{dS}{|\nabla_k(E_c - E_v)|} \quad (3)$$

where E_c and E_v are energies of CB and VB respectively. It is clearly seen from the figure that E_c and E_v at high symmetrical K and K' points follow $\nabla_k E_c = \nabla_k E_v = 0$ condition which leads to Van Hove singularity (VHS) in JDOS. As the transition probability at these K and K' points becomes maximum due to VHS, the saturation absorption appears at A and B peak positions. On the other hand, the condition $\nabla_k(E_c - E_v) = 0$ along $\Gamma - K$ direction with $|\nabla_k E_c| \sim |\nabla_k E_v| > 0$ indicates band nesting, gives rise to SA at C peak in TAS signal due to the singularities in JDOS.

F. Charge carrier decay dynamics

To investigate the excitonic quasiparticles decay dynamics, we have fitted the TAS signal with a multi-exponential decay equation containing three time constants (T_1 - T_3) along with an instrument response function (IRF) fixed at 200 fs for different probe wavelengths as shown in Fig. 7. Typically, for TMDs, the T_1 component is consigned as Auger scattering ranging in few picoseconds⁵². The 2nd and 3rd decay components (T_2 and T_3) describe the time scale of non-radiative (rapid relaxation due to surface defect states) and radiative (band-to-band transition) recombinations, respectively^{30,53}. The values of all three time constants for all six peaks of the TAS signal are tabulated in Tab. II for

Probe wavelength	C exciton	ESA	B exciton	BB biexciton	A exciton	AA biexciton
T1 (ps)	1.36 ± 0.06	2.37 ± 0.16	1.34 ± 0.05	1.64 ± 0.08	1.19 ± 0.03	1.52 ± 0.04
T2 (ps)	21.3 ± 1.9	35.9 ± 4.1	34.2 ± 20.2	42.3 ± 4.1	94.9 ± 73.4	54.4 ± 8.1
T3 (ps)	1713.3 ± 263.0	297.4 ± 21.9	95.4 ± 16.4	503.9 ± 38.6	1494.9 ± 851.0	773.8 ± 60.8

TABLE II. Non-radiative and radiative lifetimes of different excitons and biexcitons.

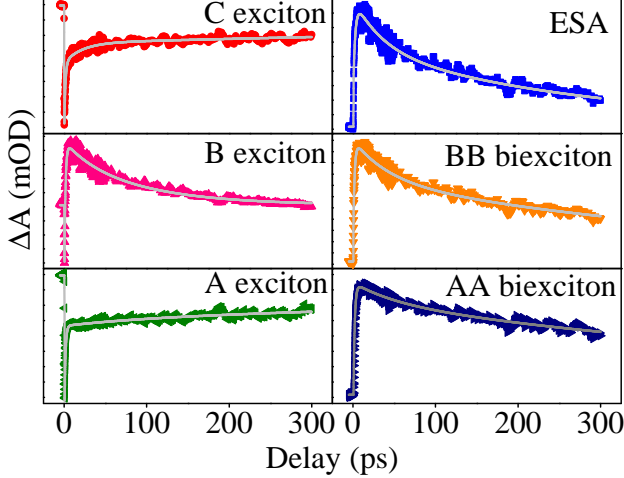


FIG. 7. (Color online) The ultrafast non-radiative and radiative lifetimes of the excitons and biexcitons are calculated using 3rd exponentially fitted TAS spectra with 200 fs instrument response function (IRF). In this figure, we have represented A, B and C excitons with olive, pink and red markers respectively. ESA is represented as blue marker whereas AA and BB biexcitons are denoted with navy blue and orange markers respectively. Grey lines are used as 3rd exponential fitting.

405 nm, 3 mW (1.8 GW/cm²) pump excitation. Interestingly, we have found that T₁ and T₂ i.e. the non-radiative decay components are similar for all kinds of excitons and biexcitons. However, the radiative component i.e. T₃ is varying depending upon different quasiparticles. We observe that A and C excitons have similar kind of decay characteristics as SAs are resonantly coupled with each other whereas there is an anomaly for T₃ of B exciton. From the TAS spectra as shown in Fig. 4, it is evident that the negative saturation absorption valley for B exciton is overwhelmed due to the presence ESA and BB biexciton. Our fitting results in a smaller decay component (T₃) of ~ 300 ps for ESA, whereas the typical radiative lifetime of exciton (T₃ of A and C) are coming out to be in the order of nanosecond. Thus, the presence of ESA may explain the reason behind the decreased radiative lifetime of B exciton. On the other hand, in the case of pump induced absorptions, the radiative decay constants of ESA are much smaller than the biexcitonic peaks which are corroborated with the previously discussed time evolution of TAS spectra (Fig. 4).

IV. DISCUSSION

In conclusion, we have established the formation and evolution of ultrafast excitonic quasiparticles (excitons and biexcitons) at room temperature and presented their decay dynamics in the solvent (DMF) exfoliated mono-to-quad layer WS₂ dispersion using optical pump (405 nm) and broadband UV-visible probe (350-750 nm). Transient absorption spectra reveal the existence of excitonic and biexcitonic features in the dispersion similar to a monolayer WS₂, as predicted by theoretical results. The first principle calculation suggests that the loss of degeneracy in both VB and CB are still prominent in the modulated layer numbers. The blue shift ($\Delta_{BB} \sim 90$ meV) of biexcitonic peak occurs due to exciton cooling process whereas pump power dependent red shifts ($\Delta_{AA} \sim 90$ meV and $\Delta_{BB} \sim 80$ meV) appear due to strong many body interactions among the quasiparticles. The binding energies of AA (~ 69 meV) and BB (~ 66 meV) biexcitons extracted experimentally that agree well with the theoretically reported layered WS₂³⁹. We have shown that the excitons act like Weiner-Mott excitons due to the dominance of short-range coulomb interactions and explained the origin of the generation of different excitons (A, B and C) via first-principles calculations as well. Moreover, from time-resolved studies, we have measured the ultrafast non-radiative and radiative lifetimes of different quasiparticles using three exponential decay processes. In summary, the detailed pump-probe spectroscopic investigation of chemically synthesized layered WS₂ provided a precious information of the excitonic quasiparticles dynamics, that can be conducive to explain the novel optical properties of this material, which may set a new paradigm for cost-effective large-scale production compatible WS₂ based device applications.

V. ACKNOWLEDGMENTS

RKC, SB and SN acknowledge MHRD, India for support. RKC acknowledge Mr. Subhojit Jana for his help in calculations. SN thanks Dr. Monodeep Chakraborty for useful discussions. RKC and SB thanks Dr. Simone Peli for his helpful inputs. Authors acknowledge SDGRI-UPM project of IIT Kharagpur for necessary equipment support in Ultrafast Science Lab, Department of Physics, IIT Kharagpur.

- ¹ Zenga, H. et al. An optical spectroscopic study on two-dimensional group-VI transition metal dichalcogenides. *Chem. Soc. Rev.* **44**, 2629 (2015).
- ² Xu, M. s. et al. Graphene-Like Two-Dimensional Materials. *Chem. Rev.* **113**, 3766 (2013).
- ³ Wang, Q. H. et al. Electronics and optoelectronics of two-dimensional transition metal dichalcogenides. *Nat. Nanotec.* **7**, 699 (2012).
- ⁴ Balandin, A. A., Thermal properties of graphene and nanostructured carbon materials. *Nat. Mater.* **10**, 569 (2011).
- ⁵ Novoselov, K. S. et al., A roadmap for graphene. *Nature* **490**, 192 (2012).
- ⁶ Kobayashi, Y. et al. Growth and Optical Properties of High-Quality Monolayer WS₂ on Graphite. *ACS Nano* **9**, 4056 (2015).
- ⁷ Kim, H.-C. et al. Engineering Optical and Electronic Properties of WS₂ by Varying the Number of Layers. *ACS Nano* **9**, 6854 (2015).
- ⁸ Schaibley, J. R. et al. Valleytronics in 2D materials. *Nat. Rev. Mats.* **1**, 16055 (2016)
- ⁹ Britnell, L. et al. Strong light-matter interactions in heterostructures of atomically thin films. *Science* **340**, 1331 (2013).
- ¹⁰ Late, D. J. et al. Hysteresis in Single-Layer MoS₂ Field Effect Transistors. *ACS Nano* **6**, 5635 (2012).
- ¹¹ Kwon, K. C. et al. Synthesis of Atomically Thin Transition Metal Disulfides for Charge Transport Layers in Optoelectronic Devices. *ACS Nano* **9**, 4146 (2015).
- ¹² Pile, D. Optical materials: Thin photovoltaics. *Nat. Photonics* **7**, 504 (2013).
- ¹³ Geim A. K. et al. The rise of graphene. *Nat. Mater.* **6**, 183 (2007).
- ¹⁴ Carvalho, A. et al. Band nesting and the optical response of two-dimensional semiconducting transition metal dichalcogenides. *Phys. Rev. B* **88**, 115205 (2013).
- ¹⁵ Schmidt, R. et al. Ultrafast Coulomb-Induced Intervalley Coupling in Atomically Thin WS₂. *Nano Lett.* **16**, 2945 (2016).
- ¹⁶ Sie, A. J. et al. Intervalley biexcitons and many-body effects in monolayer MoS₂. *Phys. Rev. B* **92**, 125417 (2015).
- ¹⁷ Sie, E. J. et al. Observation of Exciton Redshift/Blueshift Crossover in Monolayer WS₂. *Nano Lett.* **17**, 4210 (2017).
- ¹⁸ Kidd, D. W. et al. Binding energies and structures of two-dimensional excitonic complexes in transition metal dichalcogenides. *Phys. Rev. B* **93**, 125423 (2016).
- ¹⁹ Huser, F. et al. How dielectric screening in two-dimensional crystals affects the convergence of excited-state calculations: Monolayer MoS₂. *Phys. Rev. B* **88**, 245309 (2013).
- ²⁰ Wang, G. et al. Excitons in atomically thin transition metal dichalcogenides, [arXiv:1707.05863](https://arxiv.org/abs/1707.05863) (2017).
- ²¹ Aleithan, S. H. et al. Broadband femtosecond transient absorption spectroscopy for a CVD MoS₂ monolayer. *Phys. Rev. B* **94**, 035445 (2016).
- ²² Sim, S. et al. Exciton dynamics in atomically thin MoS₂: Interexcitonic interaction and broadening kinetics. *Phys. Rev. B* **88**, 075434 (2013).
- ²³ Mak, K. F. et al. Tightly bound trions in monolayer MoS₂. *Nat. Materials* **12**, 207 (2013).
- ²⁴ Zhu, B. et al. Exciton binding energy of monolayer WS₂. *Sci. Rep.* **5**, 9218 (2015).
- ²⁵ Yuan L. et al. Exciton dynamics and annihilation in WS₂ 2D semiconductors. *Nanoscale* **7**, 7402 (2015).
- ²⁶ Paradisanos, I. et al. Room temperature observation of biexcitons in exfoliated WS₂ monolayers. *Appl. Phys. Lett.* **110**, 193102 (2017).
- ²⁷ You, Y. et al. Observation of biexcitons in monolayer WSe₂. *Nature Physics* **11**, 477 (2015).
- ²⁸ Danovich, M. et al. Dark trions and biexcitons in WS₂ and WSe₂ made bright by e-e scattering. *Sci. Rep.* **7**, 45998 (2017).
- ²⁹ Chowdhury, R. K. et al. Novel silicon compatible p-WS₂ 2D/3D heterojunction devices exhibiting broadband photoreponse and superior detectivity. *Nanoscale* **8**, 13429 (2016).
- ³⁰ Chowdhury, R. K. et al. Synergistic effect of polymer encapsulated silver nanoparticle doped WS₂ sheets for plasmon enhanced 2D/3D heterojunction photodetectors. *Nanoscale* **9**, 15591 (2017).
- ³¹ Borzda, T. M. et al. Charge Photogeneration in Few-Layer MoS₂. *Adv. Funct. Mater.* **25**, 3351 (2015).
- ³² Kime, G. et al. Ultrafast Charge Dynamics in Dispersions of Monolayer MoS₂ Nanosheets. *J. Phys. Chem. C* **121**, 22415 (2017).
- ³³ Chernikov, A. et al. Exciton Binding Energy and Nonhydrogenic Rydberg Series in Monolayer WS₂. *Phys. Rev. Lett.* **113**, 076802 (2014).
- ³⁴ Vega-Mayoral, V. et al. Exciton and charge carrier dynamics in few-layer WS₂. *Nanoscale* **8**, 5428 (2016).
- ³⁵ Pogna, E. A. A. et al. Photo-Induced Bandgap Renormalization Governs the Ultrafast Response of Single-Layer MoS₂. *ACS Nano* **10**, 1182 (2016).
- ³⁶ Qiu, D. Y. et al. Optical Spectrum of MoS₂: Many-Body Effects and Diversity of Exciton States. *Phys. Rev. Lett.* **111**, 216805 (2013).
- ³⁷ Ghorai, A. et al. Exfoliation of WS₂ in the semiconducting phase using a group of lithium halides: a new method of Li intercalation. *Dalton Trans.* **45**, 14979 (2016).
- ³⁸ Berkdemir, A. et al. Identification of individual and few layers of WS₂ using Raman Spectroscopy. *Sci. Rep.* **3**, 1755 (2013).
- ³⁹ Zhang, D. K. et al. Excited Biexcitons in Transition Metal Dichalcogenides. *Nano Lett.* **15**, 7002 (2015).
- ⁴⁰ Plechinger, G. et al. Identification of excitons, trions and biexcitons in single-layer WS₂, *Phys. Status Solidi RRL* **9**, 457 (2015).
- ⁴¹ Schmitt-Rink, S. Theory of transient excitonic optical nonlinearities in semiconductor quantum-well structures. *Phys. Rev. B* **32**, 10 (1985).
- ⁴² Hulin, D. et al. Well-size dependence of exciton blue shift in GaAs multiple-quantum-well structures. *Phys. Rev. B* **33**, 6(R) (1986).
- ⁴³ Mai, C. et al. Exciton valley relaxation in a single layer of WS₂ measured by ultrafast spectroscopy. *Phys. Rev. B* **90**, 041414(R) (2014).
- ⁴⁴ Albe, K. et al. Density-functional-theory calculations of electronic band structure of single-crystal and single-layer WS₂. *Phys. Rev. B* **66**, 073413 (2002).
- ⁴⁵ Bhattacharyya, S. et al. Semiconductor-metal transition in semiconducting bilayer sheets of transition-metal dichalcogenides. *Phys. Rev. B* **86**, 075454 (2012).

- ⁴⁶ Zhu, Z. Y. et al. Giant spin-orbit-induced spin splitting in two-dimensional transition-metal dichalcogenide semiconductors. *Phys. Rev. B* **84**, 153402 (2011).
- ⁴⁷ Lu, H.-Z. et al. Intervalley Scattering and Localization Behaviors of Spin-Valley Coupled Dirac Fermions. *Phys. Rev. Lett.* **110**, 016806 (2013).
- ⁴⁸ Dou, X. et al. Probing SpinOrbit Coupling and Interlayer Coupling in Atomically Thin Molybdenum Disulfide Using Hydrostatic Pressure. *ACS Nano* **10**, 1619 (2016).
- ⁴⁹ Ye, Z. et al. Probing excitonic dark states in single-layer tungsten disulphide. *Nature* **513**, 214 (2014).
- ⁵⁰ Zhou, Y. et al. Probing dark excitons in atomically thin semiconductors via near-field coupling to surface plasmon polariton. *Nat. Nanotec.* **12**, 856860 (2017).
- ⁵¹ Liang, W. Y. et al. A study of the optical joint density-of-states function. *J. Phys. C: Solid State Phys.* **9**, (1976).
- ⁵² Cunningham, P. D. et al. Auger Recombination in Chemical Vapor Deposition-Grown Monolayer WS₂. *J. Phys. Chem. Lett.* **7**, 5242 (2016).
- ⁵³ Sun, D. et al. Observation of Rapid ExcitonExciton Annihilation in Monolayer Molybdenum Disulfide. *Nano Lett.* **14**, 5625 (2014).
- ⁵⁴ Perdew, J. P. et al. Restoring the Density-Gradient Expansion for Exchange in Solids and Surfaces. *Phys. Rev. Lett.* **100**, 136406 (2008).
- ⁵⁵ Blaha, P. et al. WIEN2K An Augmented Plane Wave + Local Orbitals Program for Calculating Crystal Properties (Karlheinz Schwarz, Techn. Universitat Wien, Austria, 2001).